AN EXPERIMENTAL STUDY ON POST-CHF HEAT TRANSFER FOR LOW FLOW OF WATER IN A 3x3 ROD BUNDLE

SANG-KI MOON*, SE-YOUNG CHUN, SEOK CHO, SE-YUN KIM and WON-PIL BAEK
Korea Atomic Energy Research Institute
150 Deokjin-dong, Yuseong-gu, Daejeon 305-353, Korea
*Corresponding author. E-mail : skmoon@kaeri.re.kr

Received February 11, 2005
Accepted for Publication May 31, 2005

An experimental study on post-CHF heat transfer has been performed with a 3x3 rod bundle using a vertical steam-water two-phase flow at low flow conditions. The effects of various parameters on the post-CHF heat transfer are investigated and the reasons for the parametric effects are discussed. As the heat transfer regime changes from CHF to post-CHF, the radial wall temperature distribution is changed depending on the pressure and the mass flux conditions. The superheat of the fluid increases considerably with an increase of the wall temperature (or heat flux) and with a decrease of the mass flux. This implies, indirectly, a strong thermal non-equilibrium at high wall temperature and low mass flux conditions. In order to improve the prediction accuracy of the existing post-CHF correlations, it is necessary to perform more experiments, particularly direct measurement of the vapor superheat, and to modify the correlation by considering a strong thermal non-equilibrium at low flow and low pressure conditions.

KEYWORDS : Post-CHF Heat Transfer, Low Flow of Water, Thermal Non-Equilibrium, 3x3 Rod Bundle

1. INTRODUCTION

The heat transfer regime encountered at heat flux levels after exceeding the critical heat flux (CHF) is generally referred to as the post-CHF (or post-dryout) regime. In the post-CHF heat transfer regime the heated surface is cooled by forced convection to vapor, interaction of the liquid and the heated surface, and radiation heat transfer., The convective heat transfer from the heated surface to a bulk vapor flow plays the most important role in the post-CHF heat transfer regime. A low heat transfer coefficient by the vapor flow results in a high surface temperature and may lead to physical damage to the heated surface. Excellent reviews on post-CHF heat transfer can be found in a textbook edited by Hewitt et al. [1] and several other articles [2, 3].

The post-CHF as well as the CHF under low flow conditions play an important role in the thermal hydraulic behavior of research reactors and advanced nuclear reactors as well as in the accident analyses of light water reactors. In light water reactors, a loss of flow transient or an overpower accident may result in exposure of at least part of the fuel rods to post-CHF conditions. At high pressure and low flow conditions, the post-CHF behavior is not well understood as of yet. This behavior is considered to be of importance in the safety of nuclear reactors during high pressure core inventory boil-off and fuel rod dryout situations, which may occur during a small break loss-of-coolant accident or an anticipated transient without scram (ATWS). Furthermore, at low pressure and low flow conditions, the post-CHF phenomena become more complex due to the important role of buoyancy forces, flow instabilities, the large specific volume of the vapor, and the combined effects of the loop design parameters. Accordingly, interest in post-CHF phenomena under low flow and low-to-high pressure conditions has been continuously growing. However, due to the complex nature and the poor prediction capacity of the existing correlations and models of post-CHF phenomena, post-CHF remains a subject of active research while the application field is steadily expanding.

Because of the importance of post-CHF heat transfer, numerous experimental and theoretical works on post-CHF heat transfer have been conducted. However, most of the experimental studies have been carried out using simple geometries such as tubes and annuli. This results from the various inherent difficulties in a post-CHF experiment using rod bundles. First, a rod bundle post-CHF experiment generally requires high wall temperature and high power. Second, the hot patch technique [4], usually used successfully in tubes, cannot be used in rod bundles

under high pressure conditions, as it requires either external cartridge heaters or very thin wall thickness in order to obtain high quality inlet conditions.

Up to the 1970s, most post-CHF experiments using rod bundles focuses on high flow conditions relevant to the light water reactor conditions [3]. From the late 1970s, several experiments were conducted on post-CHF heat transfer using a rod bundle under low flow conditions. Over the past few decades, many experiments using rod bundles have been conducted by Japanese researchers, focusing on high pressure and low flow conditions [5-7]. Koizumi et al. [5] performed post-CHF experiments using a single rod and a 5x5 rod bundle. Their experiments covered a mass flux from 20 to 800 kg/m^{2}s, and pressures from 3 to 12 MPa. They modified the Groeneveld correlation [8] by accounting for the dependence of the heat transfer on the heater wall temperature. Kumamaru et al. [6] performed a post-CHF experiment using a 5x5 rod bundle under conditions of mass flux from 80 to 320 kg/m^{2}s, and a pressure of 3 MPa. They concluded that the Varone-Rohsenow [9] prediction calculated the wall temperature relatively well for their experimental conditions. Akiyama et al. [7] conducted post-CHF experiments on a full scale boiling water reactor 8x8 rod bundle. Their experimental conditions covered a mass flux from 284 to 1562 kg/m^{2}s and a pressure of 7.15 MPa. The prediction performance of the existing correlations significantly depends on the wall superheat of the heater rod. Unal et al. [10, 11] measured the vapor superheat using a vapor superheat probe in a 3x3 rod bundle. Their experiment was carried out at a very low mass flux from 7 to 26 kg/m^{2}s under a pressure slightly above atmospheric pressure. The measured wall and vapor superheats differed in magnitude from those obtained from single tube experiments. They concluded that none of the existing non-equilibrium post-CHF heat transfer models could reasonably predict the vapor superheat and the wall heat flux simultaneously [11].

As stated above, previous post-CHF heat transfer experiments under low flow conditions concentrated on relatively high pressure conditions [3]. Thus, in this study, the post-CHF experiment has been performed under low flow and low-to-high pressure conditions. This paper presents the experimental data, discusses the parametric trends, and evaluates the applicability of the existing correlations to the rod bundle post-CHF heat transfer data under low flow and low-to-high pressure conditions.

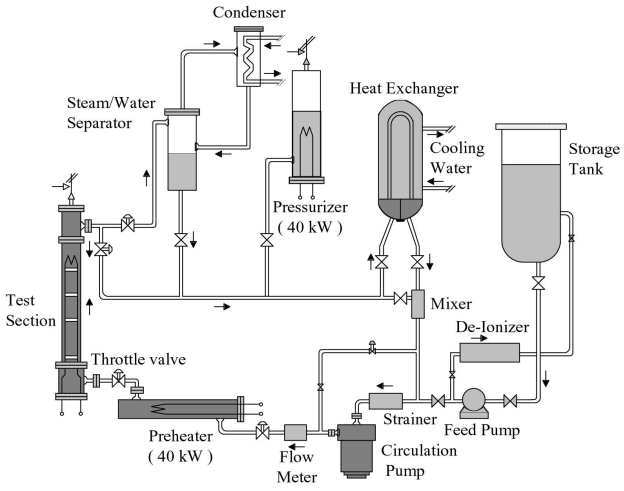

Fig. 1. KAERI RCS Thermal Hydraulic Loop

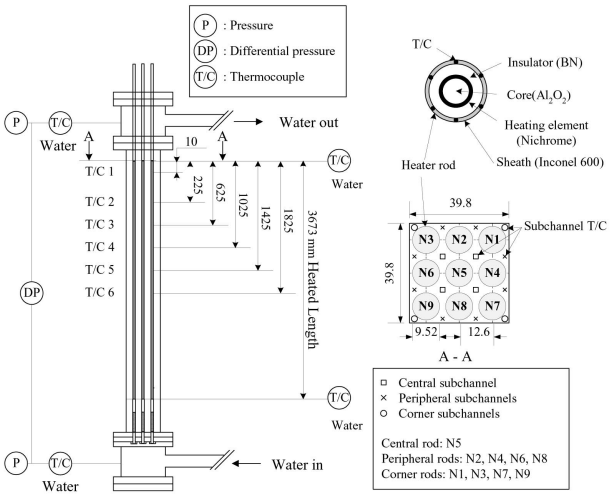

Fig. 2. Test Section and Instrumentations

2. TEST FACILITY AND TEST METHOD

2.1. Test Facility and Test Procedure

Post-CHF heat transfer experiments have been carried out in a reactor coolant system thermal hydraulic loop facility (RCS loop facility) at the Korea Atomic Energy Research Institute (KAERI). Figure 1 shows a schematic diagram of the RCS loop facility [12]. It basically consists of a main circulation pump, a preheater, a 3x3 rod bundle, a steam/water separator, a condenser, a pressurizer, and a cooler. The loop is filled with de-ionized water. The water flow rate at the test section inlet is controlled by adjustment of the motor speed of the main circulating pump and the flow control valves. The water flow rate at the test section is measured by orifices, and flow oscillations, which are usually observed at low flow conditions, are effectively suppressed by decreasing the opening of a throttle valve installed upstream of the test section until the oscillations are negligible. The preheater with a power of 40 kw adjusts the inlet subcooling of the water entering the test section. The inlet plenum pressure of the test section is maintained at nearly constant values by using the pressurizer with an

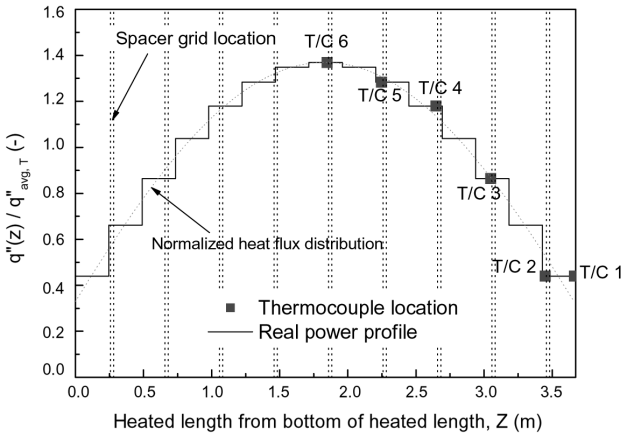

Fig. 3. Axial Heat Flux Distribution

immersion heater of 40 kW.

As shown in Fig. 2, the test section has a flow housing (39.8 x 39.8 mm^2) inside the pressure vessel where nine heater rods with a heated length of 3673 mm are located in a 3x3 square array. All the heaters, respectively having a diameter of 9.52 mm and a pitch of 12.6 mm, are heated indirectly by AC (alternating current) power. The sheath and heating element of the heater rods are made of Inconel 600 and Nichrome, respectively. Eleven spacer grids with a simple geometry are installed to support the heater rods along the axial length in the test section. The spacer grid effects on the post-CHF heat transfer are assumed to be negligible in the present experiments, since they have no mixing vanes and the thermocouples for the measurement of the wall temperature are installed just upstream of the spacer grids. Six or four K-type thermocouples with a sheath diameter of 0.5 mm are embedded on the heater rod surface to measure the heater rod surface temperature and to detect CHF occurrence. The temperature measuring points of the thermocouples are located just upstream of the spacer grids at 10, 225, 625, 1025, 1425, and 1825 mm from the top end of the heated section. Sixteen thermocouples of the same type are located in both the inlet and the outlet of the heated section to measure the subchannel fluid temperatures. The thermocouples for the measurement of the subchannel fluid temperature are inserted into stainless steel tubes with a diameter of 1.6 mm and the end tips of the thermocouples are exposed by about 3 mm to the two-phase flow from the tip of the stainless steel tube. As shown in Fig. 3, the heated section of the heater rods is evenly divided into 15 steps to simulate a symmetric cosine axial heat flux profile with minimum and maximum heat flux ratios for an average heat flux of 1.37 and 0.44, respectively. The radial power distribution is uniform since the heater rods have the same power.

All post-CHF experiments were carried out using the following procedures. After setting the water flow rate, inlet subcooling, and inlet pressure to the desired values, the electric power to the heater rods is increased gradually, in small steps. At each power level, the test parameters such as the mass flux, pressure, power, inlet temperature, and wall temperatures are stabilized for several minutes before raising the power level again. When the test parameters are judged to be sufficiently stable, they are recorded by a data acquisition system. This process continues until the maximum wall temperature is less than about 700°C in order to protect the heater rods from any physical damage due to overheating. All the measured data are averaged for 60 seconds and only data with a standard deviation of wall temperature less than $\pm$2% is included in the data analyses. In the present experiments, about 182 series of post-CHF data are obtained, as shown in Table 1.

The measured data such as the pressure, fluid temperature, mass flux, heater rod surface temperature, and power to the heater rods are recorded, processed, and stored in a data acquisition and control unit. According to a propagation error analysis based on Taylor's series method [13], the uncertainties of the measured data are estimated from the calibration of the measurement sensors and the accuracy of the related equipment. The maximum uncertainties of the measured data for the pressure, mass flux,

Table 1. Test Conditions for the Post-CHF Heat Transfer

Test parameter	Test condition
Inlet pressure, P (MPa)	1, 3, 6, 9
Mass flux, G (kg/m^{2}s)	50 ~ 453
Inlet subcooling, Δi_i (kJ/kg)	71 ~ 347
Local quality, X_e (-)	0.46 ~ 1.60
Wall superheat of heater rods, ΔT_w (= T_w-T_v) (°C)	50 ~ 512
Average test section heat flux, q''_{avg} (kW/m^2)	92 ~ 706
Total test section power, Q_T (kW)	90 ~ 698
No. of data series	182

and temperature are estimated to be less than $\pm 0.3\%$, $\pm 1.5\%$, ± 0.7 K, respectively. The uncertainties of the power measurements supplied to the heater rods are less than $\pm 1.8\%$ of the reading values. Before starting a set of experiments, pretests (i.e., heat balance test) are carried out to estimate heat loss and to check for any abnormalities from the measuring instruments. The heat loss in the heated section estimated by the pretests for several pressure conditions is less than 2% of the applied total power to the test section.

2.2. Test Data Reduction

Subchannel analysis codes are necessary to obtain accurate local flow conditions in subchannels for each heater rod, since, in general, there exist an unheated wall and some mismatch of the flow and enthalpy values between the subchannels in a rod bundle. However, it is difficult to obtain accurate local flow conditions using subchannel codes, especially in a dispersed flow regime. Therefore, in this study, cross-sectional averaged parameters such as the equilibrium quality and mass flux are used to analyze the post-CHF heat transfer. In the post-CHF heat transfer regime, the vapor temperature can be well above the saturation temperature, resulting in a thermal non-equilibrium between the liquid and vapor phases. In particular, there is generally strong thermal non-equilibrium at low flow conditions. Under the thermal non-equilibrium conditions, the actual vapor quality is not equal to the equilibrium quality [2, 3]. Unfortunately, it is difficult to accurately measure the vapor temperature in the post-CHF heat transfer regime due to the effects of entrained liquid droplets. Although the subchannel fluid temperatures were measured in the present experiment near the exit of the test section, the vapor temperature or vapor superheat evaluated by the heat balance is used for the analysis of the post-CHF heat transfer.

Assuming a thermal equilibrium state, the cross-sectional average equilibrium quality, *Xe*, at any axial location Z is calculated by a heat balance equation using the inlet water temperature, mass flux, system pressure, and test section power from the inlet to the axial location. If the equilibrium quality has a value between 0 and 1, it is assumed that the vapor and liquid temperatures are equal to the saturation temperature. If the equilibrium quality is greater than 1, the superheated vapor temperature is calculated from the heat balance equation as follows:

$$T_v = T_l = T_{sat}(P), \quad \text{for } 0 \le X_e \le 1, \tag{1}$$

$$T_v = f(P, i_v),\ i_v(P) = X_e i_{fg}(P) + i_l(P),\ \text{for } X_e \ge 1. \tag{2}$$

The superheated vapor temperature, T_v, is calculated by using the steam tables for a given pressure, P, and superheated vapor enthalpy, i_v.

The heat transfer coefficient in the post-CHF heat transfer regime is obtained by using the net local convective heat flux, and wall and steam temperatures, by the following equations:

$$h_m = q''_{con}/(T_w - T_{sat}), \quad \text{for } 0 \le X_e \le 1, \tag{3}$$

$$h_m = q''_{con}/(T_w - T_v), \quad \text{for } X_e \ge 1, \tag{4}$$

where $q''_{con} = q''_w - q''_{rad}$. (5)

q''_{con} represents the net local convective heat flux excluding the radiation heat transfer rate from the local wall heat flux. In general, it is difficult to assess the radiation heat transfer rate for a rod bundle with a complex geometry and there is little data about the heater surface, vapor, and liquid properties related to radiation heat transfer. Thus, in this study, the radiation heat transfer is calculated by the following equations by considering only the radiation heat transfer between the heater rod and the vapor [6, 14]:

$$q''_{rad} = \varepsilon' \sigma (T_w^4 - T_v^4) \tag{6}$$

$$\varepsilon' = \left(1/\varepsilon_w + 1/\alpha_g - 1\right)^{-1} \tag{7}$$

It is assumed that the heater rods have a surface emissivity of 0.84 for the sheath material of Inconel 600. Steam absorptivity, α_g, is assumed to be equal to the steam emissivity and is obtained from the Hottel's graph [14] for each system pressure. The Hottel's graph provides the steam emissivity as a function of the pressure, the mean beam length, and the vapor temperature. The mean beam length is assumed to be equal to the hydraulic diameter [14].

The radiation heat transfer rate is small when compared to the local wall heat flux, in most cases less than 7% of the local wall heat flux, and it does not change considerably with the radiation properties of the heater rod surface and the vapor. The radiation heat transfer rate is very small except for at conditions involving a very low mass flux and high wall temperature.

As mentioned above, there exist some differences in the radiation heat transfer, flow rate, and enthalpy between the subchannels. In addition, the heater wall temperature and heat transfer coefficient depend on the location of the heater rod in the rod bundle geometry. Thus, in this study, the post-CHF heat transfer is analyzed mainly for the central rod of the test section (heater rod No. 5, see Fig. 2) located in the center of the test section.

3. TEST RESULTS AND DISCUSSION

3.1. Post-CHF Heat Transfer

Figure 4 shows the typical wall temperature and heat transfer coefficient for thermocouple No. 2 of the central

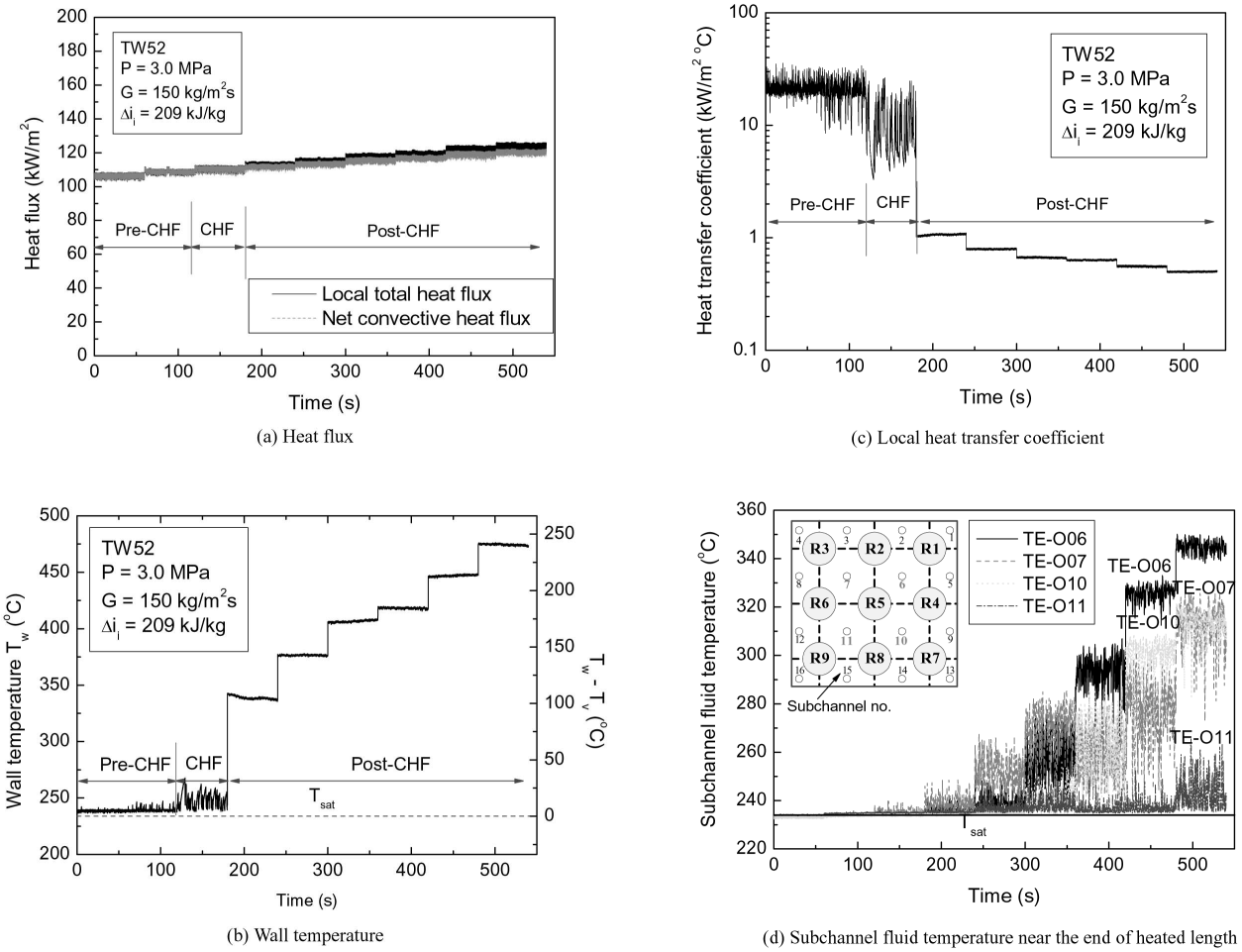

Fig. 4. Typical wall Temperature and Heat Transfer Trends

rod, where TW52 denotes the wall temperature at rod number 5 and axial thermocouple number 2 (see Figs. 2 and 3). The test section power is gradually increased, in small steps, while maintaining the pressure, mass flux, and inlet subcooling at constant values. At each power level, if the wall temperatures (except for the CHF occurrence) and other test parameters show steady state values, the data acquisition system records all the experimental parameters, including the wall temperatures, for 60 seconds. Thus, Fig. 4 does not show continuously time-based experimental data, but only steady state data at each power level. As shown in Fig. 4 (a), the radiation heat transfer is so negligible that most of the local wall heat flux contributes to the convective heat transfer. As shown in Figs. 4. (b) and (c), as the heat transfer regime changes from pre-CHF to post-CHF through the CHF occurrence, a sharp decrease in the heat transfer rate is observed due to a deterioration of the direct liquid-wall contacts. This change is indicated by a sharp increase in the wall temperature. In the pre-CHF regime, the wall temperature is close to the saturation temperature due to the high heat transfer coefficients, as shown in Fig. 4 (b). Near the CHF regime, the wall superheat becomes relatively large and the wall temperature oscillates due to repeated dryout and rewetting of the heated surface. In the post-CHF regime, the wall superheat is very large and the heat transfer coefficient is reduced to a very small value. The oscillation of the wall temperature disappears, indicating a stable film boiling. For the present experimental conditions, most of the CHFs occurred due to liquid film dryout at high quality conditions [15]. Thus, the post-CHF heat transfer regime would most likely be a dispersed flow film boiling, which is characterized by the existence of discrete liquid droplets entrained in a continuous vapor flow. Since at high quality and high wall temperature, the liquid droplets have reduced likelihood of directly contacting the hot wall, convective heat transfer by the vapor is expected to be the dominant heat transfer mode, as exhibited from the non-oscillating or the smooth trends of the wall

temperature for a given power input.

The vapor temperature in the post-CHF heat transfer regime is mainly controlled by vapor heating through convective heat transport from the wall and vapor-liquid heat exchange. Significant vapor superheats have been measured in several experiments [10, 16, 17]. This thermal non-equilibrium has a significant effect on the convective heat transfer in the post-CHF heat transfer regime. For the test conditions of Fig. 4, when assuming thermal equilibrium, the vapor temperatures calculated by the heat balance equation are nearly the same as the saturation temperature, and the maximum equilibrium quality at the exit of the test section is about 1.05. However, as shown in Fig. 4 (d), the fluid temperatures at the outlet subchannels around heater rod No. 5 become larger than the saturation temperature as the heat flux increases. The superheat of the fluid increases considerably with an increase of the wall temperature (or heat flux) and with a decrease of the mass flux. Although it is difficult to define the measured fluid temperature as the actual steam temperature due to the possible influence of liquid droplets on the measured fluid temperature, this figure indirectly represents a thermal non-equilibrium state, where the actual steam temperature is considerably greater than the saturation temperature.

In the experiment, the heater rods have the same power and hence the radial power distribution is uniform. However, at the same elevation, it is observed that some rods experience a dryout while some rods are still wetted. The scatter in the post-CHF heater wall temperature increases with increased rod bundle geometry complexity and decreased mass flux [4, 5]. Scatter might also occur as a result of imbalances in the flow rate, quality, and vapor temperature in the tightly packed multi rod bundle. Test results by Koizumi [4] show that the wall temperatures for the same radial location (i.e., center, corner or peripheral) have quite large scatterings. This scattering in the heater wall temperature may result in asymmetrical subchannel temperature, as shown in Fig. 4(d).

Figure 5 shows the axial variation of the wall superheat and the heat transfer coefficient of the central rod (rod No. 5) with varying total power of the test section at constant pressure, mass flux, and inlet subcooling. As the ratio of the total power to the first CHF power, Q_C, increases, the CHF location moves towards the upstream region. The heat transfer coefficient sharply decreases at the CHF location and subsequently increases slightly due to increased heat transfer by the vapor near the exit. The heat transfer coefficient at high power ratios decreases while the wall temperature decreases, as the elevation changes from 3 m to 3.5 m. This is a result of the large decrease in the heat flux, when compared with the decrease of the wall temperature between the two elevations (see Figs. 2 and 3).

As mentioned earlier, the heater rod wall and subchannel fluid temperatures depend on the radial locations in the rod bundle geometry. Figures 6 (a) and (b) show the average wall temperatures according to the radial location (i.e.,

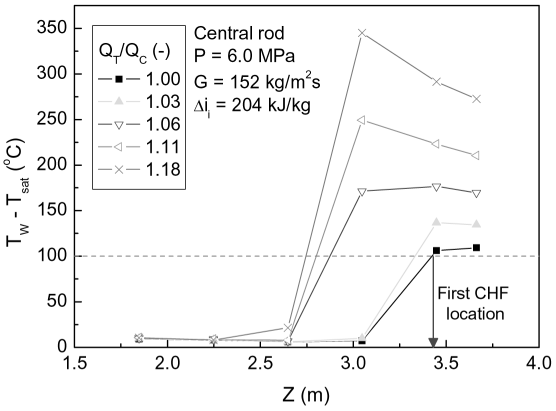

(a) Wall superheat

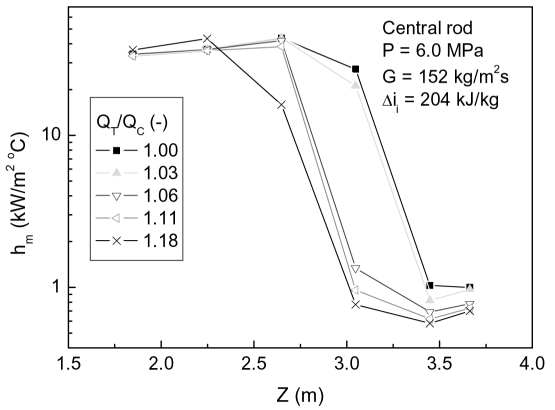

(b) Heat transfer coefficient

Fig. 5. Wall Superheat and Heat Transfer Coefficient with a Total Power

central, peripheral, and corner locations, see Fig. 2) along the axial location. For high pressure conditions greater than 6.0 MPa, near the CHF region, the average wall temperature at the corner region is higher than that of the central rod (cold wall effect). On the contrary, at low pressure conditions of 1.0 MPa, the central rod has a higher wall temperature near the CHF region relative to those of the corner and peripheral rods, except for at a very low mass flux of 50 kg/m²s. In general, the wall temperature at the peripheral rods is similar to or smaller than that of the corner rods. At the downstream of the CHF location (i.e., post-CHF regime), the wall temperature of the central rod is always larger than that of the corner and peripheral regions. Therefore, the radial wall temperature distribution is changed as the heat transfer regime changes from a CHF to a post-CHF regime. Thus, this change depends on the pressure and the mass flux. The central rod has the largest subchannel fluid temperature in the post-CHF regime, as shown in Fig. 6 (c). The subchannel fluid temperature increases by increasing the ratio of the total power of the first CHF power.

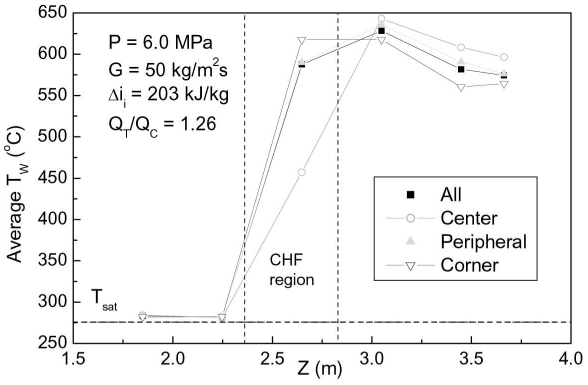

(a) Average wall temperature distribution (P = 6.0 MPa)

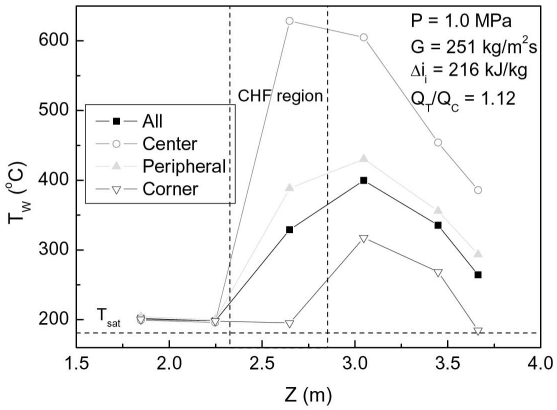

(b) Average wall temperature distribution (P = 1.0 MPa)

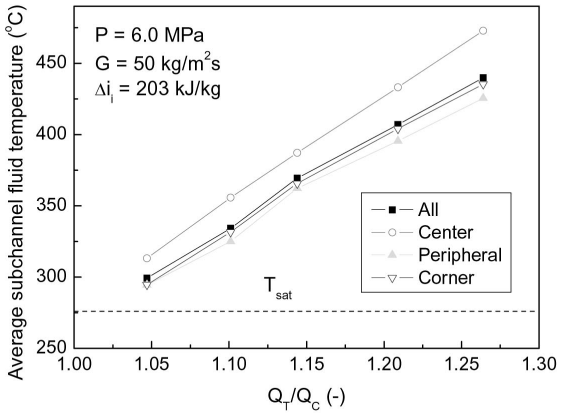

(c) Average subchannel fluid temperature

Fig. 6. Wall and Fluid Temperature Distribution

Figure 7 shows the effects of pressure on the post-CHF heat transfer coefficients at fixed mass flux and inlet subcooling conditions. The heat transfer coefficient decreases with an increase in the temperature difference

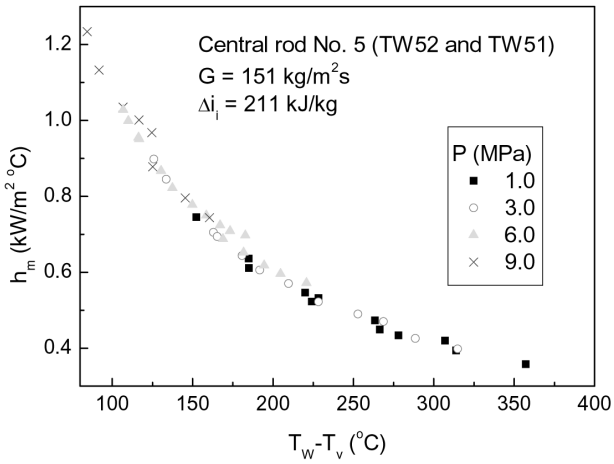

Fig. 7. Effects of the Pressure and Wall Superheat on the Heat Transfer Coefficient

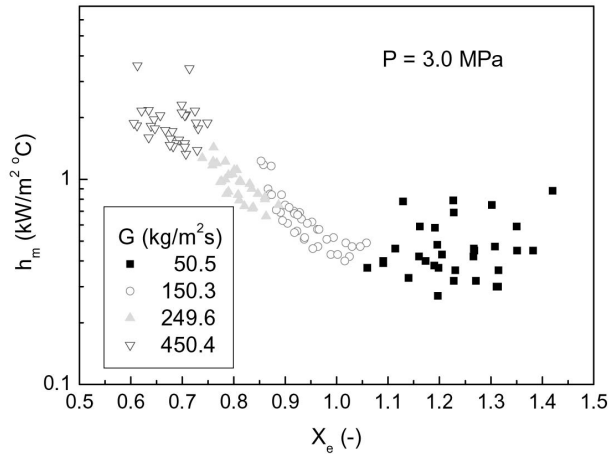

Fig. 8. Effects of the Equilibrium Quality and the Mass Flux

between the wall and the vapor, and with an increase in pressure. Interestingly, the heat transfer coefficients plot into a single unique curve regardless of the pressure. The heat transfer characteristics of the vapor improve with increased pressure as follows. The increased Prandtl number increases the convective heat transfer from the wall to the vapor. Also, the decreased viscosity of the vapor increases the turbulence of the vapor and hence increases the convective heat transfer to the vapor. Finally, a decrease of the surface tension results in smaller droplets and hence a greater interfacial area of the vapor-to-droplet heat transfer.

It is known that any increase or decrease of heat transfer with an increase of the equilibrium quality primarily depends on the mass flux and the pressure. As shown in Fig. 8, the heat transfer coefficient decreases with increasing

equilibrium quality under the present experimental conditions. However, at very low flow conditions, the effect of the vapor quality is not clear. The heat transfer coefficient increases with an increase in the quality at high mass flux conditions. On the other hand, at low mass flux conditions, the heat transfer coefficient decreases with an increase in the quality. This may be attributed to changes in the droplet concentration. Under low mass flux conditions, droplet induced turbulence and possible droplet-wall interactions might considerably affect the convective heat transfer to the vapor, when compared with the high mass flux conditions. Thus, as the quality increases, the droplet concentration decreases, and hence the heat transfer decreases with an increase in the quality.

Figure 9 shows that the heat transfer coefficient increases with the Reynolds number of the steam. The vapor velocity increases with the vapor Reynolds number, and consequently the heat transfer coefficient increases with an increase in the vapor Reynolds number.

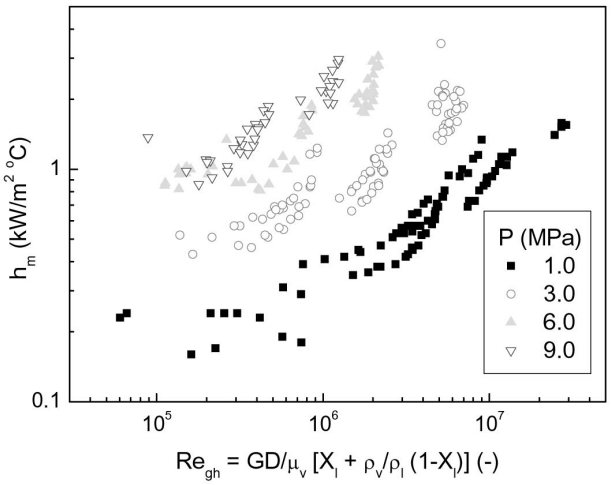

Fig. 9. Effects of the Vapor Reynolds Number and the Pressure

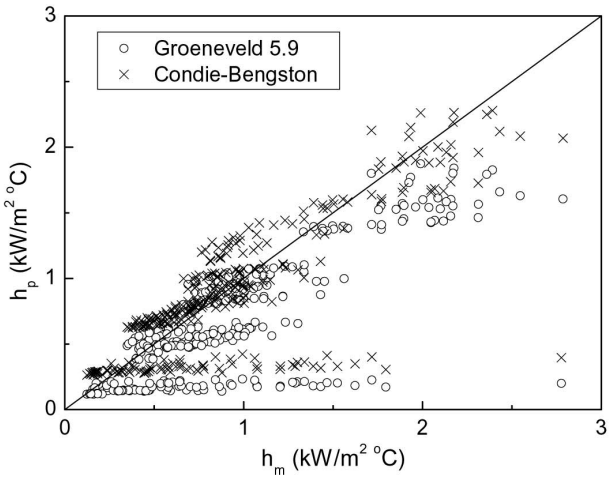

(a) Heat transfer coefficient

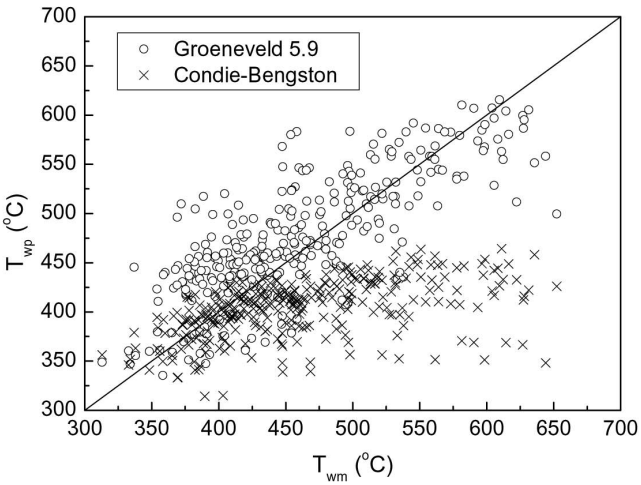

(b) Wall temperature

Fig. 10. Prediction Results of the Post-CHF Heat Transfer Correlations

3.2. Comparison with Several Correlations

Most of the existing empirical correlations of post-CHF heat transfer are equilibrium models, where the bulk vapor temperature is assumed to be equal to the local saturation temperature. Generally, these correlations use a modified equation of the Dittus-Boelter type and the heat transfer coefficient is calculated as a function of the mass flux, equilibrium quality, and saturated vapor properties. Typical equilibrium correlations are those of Dougall-Rohsenow [18], Groeneveld [8], and Condie-Bengston [19].

Thermal non-equilibrium correlations consider the vapor superheat, where the superheated vapor coexists with entrained liquid droplets. Thus, in contrast to the equilibrium correlations, the heat flux is calculated based on the difference between the wall and the superheated vapor temperature. A typical non-equilibrium correlation is that of Groeneveld-Delrome [20]. Recently, Groeneveld et al. [21] derived an improved look-up table for film-boiling heat transfer coefficients by using a world-wide post -CHF database. A comparison of the prediction accuracy of the look-up table with other prediction methods showed the look-up table yielded the best prediction results [21]. Table 2 shows the existing post-CHF heat transfer correlations.

In Fig. 10 and Table 3, the post-CHF heat transfer coefficients obtained in the present experiment are compared with the existing post-CHF heat transfer correlations, although these correlations were mainly developed using a tube database. The Dougall-Rohsenow correlation considerably overestimates the heat transfer coefficients, and hence

Table 2. Post-CHF Heat Transfer Correlations

Post-CHF heat transfer correlations
Dougall-Rohsenow [18] $h = 0.023(k_v / D)\left[\mathrm{Re}_v\left(X_l + \frac{\rho_v}{\rho_l}(1-X_l)\right)\right]^{0.8} \mathrm{Pr}_v^{0.4}$ where X_l = true equilibrium vapor weight fraction, $\mathrm{Re}_v = \frac{GD}{\mu_v}$ $X_l = X_e$, if $0 < X_e < 1$ $X_l = 1$, if $X_e > 1$
Groeneveld 5.9 [8] $h = 0.0327(k_v / D)\left[\mathrm{Re}_v\left(X_l + \frac{\rho_v}{\rho_l}(1-X_l)\right)\right]^{0.901} \mathrm{Pr}_w^{1.32}\, Y^{-1.5}$ where $Y = 1.0 - 0.1\left(\frac{\rho_l}{\rho_v} - 1\right)^{0.4}(1-X_l)^{0.4}$
Condie-Bengston [19] $h = 0.05345 \cdot 10^{-3} \frac{(k_v \times 1000)^{0.4593}\, \mathrm{Pr}_w^{2.2598}\, \mathrm{Re}_v^{[0.6249+0.2043\ln(X_l+1)]}}{D^{0.8095}(X_l+1)^{2.0514}}$
Groeneveld and Delrome [20] $h = 0.008348(k_{vf} / D)\left[\frac{GD}{\mu_{vf}}\left(X_a + \frac{\rho_v}{\rho_l}(1-X_a)\right)\right]^{0.8774} \mathrm{Pr}_{vf}^{0.6112}$ where $\frac{X_a}{X_l} = \frac{i_{fg}}{i_v(P,T_{va}) - i_{lsat}}$, $\frac{i_v(P,T_{va}) - i_v(P,T_{sat})}{i_{fg}} = \exp[-\tan\psi]\exp[-(3\alpha_{\mathrm{hom}})^{-4}]$ $\psi = a_1 \mathrm{Pr}_v^{a2}\, \mathrm{Re}_{\mathrm{hom}}^{a3}\left(\frac{q'' DC_{p_{ve}}}{k_{ve} i_{fg}}\right)^{a4} \sum_{j=0}^{2} b_j (X_l)^j$ for $0 \le \psi \le \pi/2$ $\alpha_{\mathrm{hom}} = X_l / \left(X_l + \frac{\rho_v}{\rho_l}(1-X_l)\right)$, $\mathrm{Re}_{\mathrm{hom}} = \frac{GD}{\mu_{ve}}\left(X_l + \frac{\rho_v}{\rho_l}(1-X_l)\right)$ $a_1 = 0.13864$ $a_2 = 0.2031$ $a_3 = 0.2006$ $a_4 = -0.09232$ $b_0 = 1.3072$ $b_1 = -1.0833$ $b_2 = 0.8455$

underestimates the wall temperature. While the Groeneveld 5.9 correlation underestimates the heat transfer coefficients at very low mass flux conditions, it shows the best prediction of the wall temperature with a RMS deviation of 48.17℃. The Condie-Bengston correlation has similar prediction errors, and shows reasonable predictions for both the heat transfer coefficient and the wall temperature. The prediction accuracy by the look-up table worsens as the mass flux

Table 3. Post-CHF Prediction Results by the Existing Correlations

Correlation	Heat transfer coefficient[1)]		Wall temperature[2)]	
	Average error (-)	RMS error (-)	Average deviation (°C)	RMS deviation (°C)
Dougall-Rohsenow	0.511	0.768	-101.86	126.36
Groeneveld 5.9	-0.257	0.396	16.97	48.17
Condie-Bengston	0.042	0.370	-57.64	85.29
Look-up table	-0.044	0.417	22.28	93.63
Groeneveld and Delrome	-0.143	0.365	156.01(26.39)[3]	175.11 (67.73)[3]

1) Statistics for the prediction of the heat transfer coefficient:

Error: ε = (predicted value/measured value - 1)

Average error = $\frac{1}{N}\sum_{i=1}^{N}\varepsilon_i$, RMS error = $\sqrt{\frac{1}{N}\sum_{i=1}^{N}\varepsilon_i^2}$, where N = no. of data

2) Statistics for the wall temperature prediction:

Deviation: d = predicted value - measured value

Average deviation = $\frac{1}{N}\sum_{i=1}^{N}d_i$, RMS deviation = $\sqrt{\frac{1}{N}\sum_{i=1}^{N}d_i^2}$, where N = no. of data

3) Predicted by the vapor temperature calculated from a heat balance equation

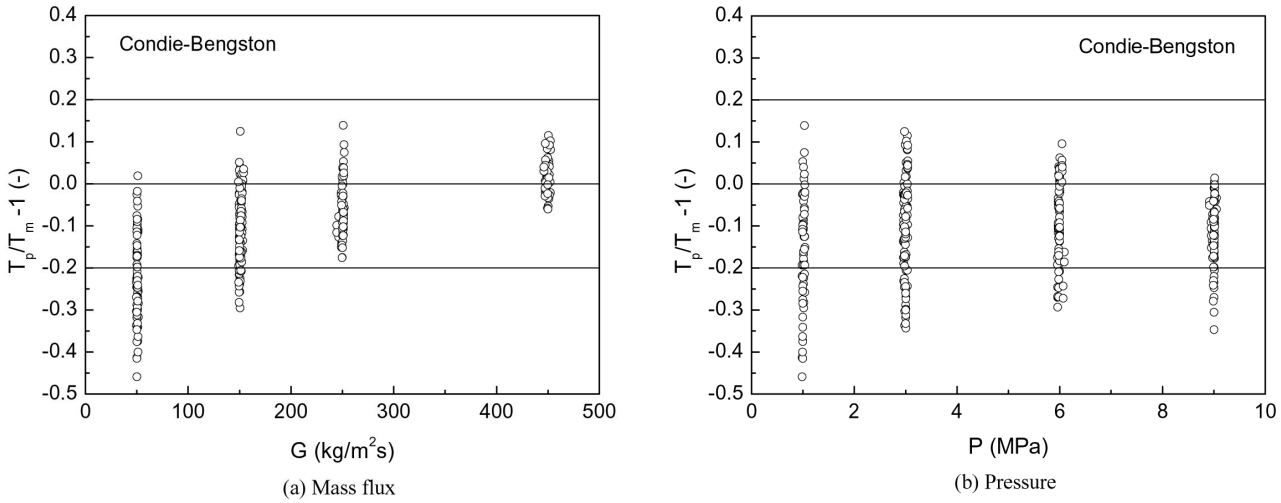

(a) Mass flux (b) Pressure

Fig. 11. Wall Temperature Prediction Results by the Condie-Bengston Correlation

and the system pressure are lowered. The non-equilibrium correlation of Groeneveld-Delrome underestimates the heat transfer coefficients while it has the smallest RMS error of 36.5%. The correlation considerably overestimates the wall temperature when the vapor temperature predicted by the correlation is used for the calculation of the wall temperature. However, interestingly, if we use the vapor temperature calculated by a heat balance equation, the average deviation and RMS deviation are 26.39°C and 67.73°C for the prediction of the wall temperature, respectively.

In general, the prediction errors by these correlations worsen at very low flow (or high quality) and low pressure conditions. As shown in Fig. 11, the prediction results by

the Condie-Bengston correlation largely depend on the pressure and the mass flux conditions. The extremely poor prediction at the low flow and low pressure conditions might be attributed to a significant thermal non-equilibrium as the mass flux and the pressure decrease. Thus, in order to improve the prediction accuracy of the existing post-CHF correlations, it is necessary to perform more experiments, particularly measurement of the vapor superheat, and to modify the correlations for low flow and low pressure conditions by considering a strong thermal non-equilibrium. The failure of these correlations to show reliable prediction results in low flow and low pressure conditions might also be attributed to the difference between the tube and rod bundle geometry. Specifically, in a rod bundle, the flow and enthalpy imbalances, and the asymmetry between the subchannels becomes large at low flow and low pressure conditions.

4. CONCLUSIONS

Using a 3x3 rod bundle with a symmetric cosine axial heat flux distribution, a post-CHF experiment has been performed at low flow conditions. From the post-CHF heat transfer experiment, the following conclusions are obtained:

(1) As the heat transfer regime changes from a CHF to a post-CHF regime, the radial wall temperature distribution is changed. Near the CHF region, the cold wall effect (higher wall temperature at the corner and peripheral regions) is observed depending on the pressure and mass flux conditions. In the post-CHF regime, the central rod has the largest wall and subchannel fluid temperatures.

(2) The fluid temperatures at the subchannel near the exit of the test section show a larger value than the saturation temperature, and the superheat of the fluid increases considerably with an increase in the wall temperature and with a decrease in the mass flux. This implies, indirectly, that the thermal non-equilibrium state becomes larger at high wall temperature and low mass flux conditions.

(3) The post-CHF heat transfer coefficient increases with increases in the steam Reynolds number and pressure. It also increases with decreased wall superheat and quality. The decrease of the heat transfer coefficient with an increase in the quality may be attributed to changes in the droplet induced turbulence and possible droplet-wall interaction with the quality.

(4) The Groeneveld 5.9 and Condie-Bengston correlations show reasonable predictions for the wall temperature. However, the prediction accuracies deteriorate as the mass flux and pressure decrease. This might be attributed to a significant thermal non-equilibrium as the mass flux and the pressure decrease. Another reason is that the flow and enthalpy imbalances, and the asymmetry in the subchannels becomes large in the rod bundle as the mass flux and the pressure decrease.

(5) In order to improve the prediction accuracy of the post-CHF correlations, it is necessary to perform more experiments, particularly direct measurement of the vapor superheat, and to modify the correlations by considering a strong thermal non-equilibrium at low flow and low pressure conditions.

Nomenclature

α	void fraction (-)
α_g	absorptivity of steam (-)
C_p	specific heat (kJ/kg-°C)
D	hydraulic diameter (m)
d	prediction deviation for the wall temperature (°C)
Δi_i	inlet subcooling (kJ/kg)
ΔT_w	wall superheat (T_w - T_{sat}) (°C)
ε	prediction error for the heat transfer coefficient (-)
ε_w	emissivity of the heater surface (-)
$\acute{\varepsilon}$	effective emissivity (-)
G	mass flux (kg/m^{2}s)
h	heat transfer coefficient (kW/m^2-°C)
i	enthalpy (kJ/kg)
i_{fg}	latent heat of vaporization (kJ/kg)
k	thermal conductivity (kW/m-°C)
μ	viscosity (N-s/m^2)
P	pressure (MPa)
Pr	Prandtl number (-)
Re_v	Reynolds number of steam (= GD/μ_v) (-)
Re_{gh}	Reynolds number of steam (homogeneous) (-)
ρ	density (kg/m^3)
Q_C	the first CHF power (critical power) for the whole test section (kW)
Q_T	total test section power (kW)
q''	heat flux (kW/m^2)
σ	Stefan-Boltzmann constant (=5.669 x10^{-11} kW/m^2 °C^4)
T_l	liquid temperature (°C)
T_{sat}	saturation temperature (°C)
T_v	vapor temperature (°C)
X_a	actual quality (-)
X_e	equilibrium quality (-)
X_l	true equilibrium vapor weight fraction (-)
Z	axial distance from bottom of heated length (m)

subscripts

a	actual
avg	test section average
C	critical heat flux
con	convective heat transfer
e	equilibrium
f	properties evaluated at film
g	saturated vapor
hom	homogeneous
l	saturated liquid
m	measured
p	predicted
rad	radiation heat transfer

sat	saturation
T	total
v	vapor
w	wall

Acknowledgements

This work was performed under the Long-Term Nuclear R&D Program sponsored by the Ministry of Science and Technology of Korea.

REFERENCES

[1] G. F. Hewitt, J. M. Delhaye and N. Zuber, *Post Dryout Heat Transfer*, CRC Press, Inc., Boca Raton, Florida (1992).
[2] J. C. Chen, "A Short Review of Dispersed Flow Heat Transfer in Post-Dryout Boiling," *Nucl. Eng. Design*, **95**, 375 (1986).
[3] D. C. Groeneveld, "Post-Dryout Heat Transfer: Physical Mechanisms and a Survey of Prediction Methods," *Nucl. Eng. Design*, **32**, 283 (1975).
[4] D. C. Groeneveld and S. R. M Gardiner, "A Method of Obtaining Flow Film Boiling Data for Subcooled Water," *Int. J. Heat Mass Transfer*, **21**, 17 (1978).
[5] Y. Koizumi, H. Kumamaru, T. Yonomoto and K. Tasaka, "Post-Dryout Heat Transfer of High-Pressure Steam-Water Two-Phase Flow in Single Rod Channel and Multi Rod Bundle," *Nucl. Eng. Design*, **99**, 157 (1987).
[6] H. Kumamaru, Y. Koizumi and K. Tasaka, "Investigation of Pre- and Post-Dryout Heat Transfer of Steam-Water Two-Phase Flow in a Rod Bundle," *Nucl. Eng. Design*, **102**, 71 (1987).
[7] M. Akiyama, A. Inoue, M. Ohishi et al., "Study on Post-BT Heat Transfer in a Full Scale BWR (8x8) Rod Bundle," *Nucl. Eng. Design*, **117**, 341 (1989).
[8] D. C. Groeneveld, "Post-Dryout Heat Transfer at Reactor Operating Conditions," AECL-3281, Atomic Energy of Canada Limited (1973).
[9] A. F. Varone and W. M. Rohsenow, "Post Dryout Heat Transfer Prediction," *Proc. of the Joint Japan-USA Two-Phase Flow Conf*., Lake Placid, New York, USA, Aug. (1984).
[10] C. Unal, K. Tuzla, J. C. Chen, S. Neti and O. Badr, "Convective Film Boiling in a Rod Bundle: Axial Variation of Nonequilibrium Evaporation Rates," *Int. J. Heat Mass Transfer*, **31**[10], 2091 (1988).
[11] C. Unal, K. Tuzla, A. F. Cokmez-Tuzla and J. C. Chen, "Vapor Generation Rate Model for Dispersed Drop Flow," *Nucl. Eng. Design*, **125**, 161 (1991).
[12] S. Y. Chun, S. K. Moon, H. J. Chung, M. K. Chung and M. Aritomi, "An Experimental Study on Heat Transfer Characteristics Just Before Critical Heat Flux in Uniformly Heated Vertical Annulus Under a Wide Range of Pressures," *J. of the Korean Nuclear Society*, **34**[4], 269 (2002).
[13] ANSI/ASME PTC 19.1, ASME *Performance Test Codes, Supplement on Instruments and Apparatus, Part 1, Measurement Uncertainty*, ASME, New York (1985).
[14] H. C. Hottel and A. F. Sarofim, *Radiative Transfer*, McGraw-Hill, New York (1967).
[15] S. K. Moon, S. Y. Chun, S. Cho, J. K. Park and W. P. Baek, "An Experimental Study on the Low Flow CHF in Vertical Rod Bundle with Non-Uniform Axial Heat Flux Distribution," *Proc. of the 10th Int. Topical Meeting on Nuclear Thermal Hydraulics* (*NURETH-10*), Seoul, Korea, Oct. 5-11 (2003).
[16] D. Evans, S. W. Webb and J. C. Chen, "Axially Varying Vapor Superheats in Convective Film Boiling," *Journal of Heat Transfer*, **107**, 663 (1985).
[17] S. Nijhawan, J. C. Chen, R. K. Sundaram and E. J. London, "Measurement of Vapor Superheat in Post-Critical-Heat-Flux Boiling," *Journal of Heat Transfer*, **102**, 465 (1980).
[18] R. S. Dougall and W. M. Rohsenow, "Film Boiling on the Inside of Vertical Tubes with Upward Flow of the Fluid at Low Qualities," MIT Report No. 9079-26, Massachusetts Institute of Technology (1963).
[19] K. G. Condie, S. J. Bengston and S. L. Richlein, "Measurement of Axially Varying Nonequilibrium in Post-Critical-Heat-Flux Boiling in a Vertical Tube," NUREG/CR-3362, U.S. Nuclear Regulatory Commission (1983).
[20] D. C. Groeneveld and G. G. J. Delorme, "Prediction of Thermal Non-Equilibrium in the Post-Dryout Regime," *Nucl. Eng. Design*, **36**, 17 (1976).
[21] D. C. Groeneveld, L. K. H. Leung et al., "A Look-Up Table for Fully Developed Film-Boiling Heat Transfer," *Nucl. Eng. Design*, **225**, 83 (2003).